HIGHLIGHT

Check for updates

Graphene-based thermoelectric materials: toward sustainable energy-harvesting systems

Jewook Kim,†[a] Hwanseok Chang,†[a] Gwangmin Bae,[a] Myungwoo Choi*[b] and Seokwoo Jeon [iD] *[a]

Among sustainable energy-harvesting systems, thermoelectric technology has attracted considerable attention because of its ability to directly convert heat into electricity and diverse applications. Graphene, with its exceptional electrical conductivity and mechanical properties, is a promising candidate for thermoelectric materials. However, efficient thermoelectric applications require materials with a high Seebeck coefficient and low thermal conductivity—criteria that graphene does not inherently satisfy, owing to its gapless energy band structure and ballistic thermal conduction. This review examines the thermoelectric properties of graphene, optimization strategies, and the potential of graphene hybridization for thermoelectric applications. To overcome the intrinsic limitations of graphene for thermoelectric utilization, nanostructuring strategies based on its synthesis methods are discussed. Furthermore, strategies for graphene hybridization are introduced, with a focus on maximizing thermoelectric efficiency through interactions with nanostructured materials of various dimensions. Finally, the potential of graphene-based thermoelectric materials and future research directions are discussed.

1. Introduction

The rapid increase in global energy demand, coupled with the depletion of fossil fuels, has heightened concerns about environmental pollution and climate change. To address these challenges, considerable attention has been directed toward the development of sustainable and efficient energy-harvesting technologies, such as solar cells,[1–3] piezoelectric generators,[4,5] triboelectric generators,[6–8] and thermoelectric systems.[9–14] Among these technologies, thermoelectric systems have attracted increasing attention for their ability to directly convert waste heat into electricity. This unique property makes them highly versatile for applications in aerospace engineering,[15–17] automotive engineering,[18–20] body-heat harvesting,[21–23] and thermal management systems.[24–26] Thermoelectric systems achieve energy conversion through the Seebeck effect, and their efficiency is evaluated using the dimensionless figure of merit ($zT = \sigma S^2 T/\kappa$), where σ represents the electrical conductivity, S is the Seebeck coefficient, T represents the absolute temperature, and κ represents the thermal conductivity. The total thermal conductivity (κ) consists of contributions from electrons (κ_e) and phonons (κ_{ph}).

Generally, for conventional bulk thermoelectric materials, the fundamental limitation arising from tradeoffs among thermoelectric parameters inhibits performance enhancement.[27,28] For example, a reduction in thermal conductivity often suppresses electrical conductivity, limiting performance. Nonetheless, significant progress has been made in recent years with the advent of advanced materials and innovative strategies, such as nanostructuring,[14,29,30] grain-boundary engineering,[31–33] and composite approaches.[34–36]

Since its discovery in 2004, graphene has attracted considerable research interest owing to its high electrical conductivity,[37] carrier mobility,[38] mechanical strength,[39] and flexibility.[40] These outstanding electrical properties have led to its primary applications in energy storage systems—particularly as an anode material for lithium-ion batteries.[41] Additionally, its large surface area and tunable surface chemistry have enabled its use as an absorbent material for environmental remediation.[42] Beyond these primary applications, graphene has emerged as a promising candidate for thermoelectric materials, driven by its superior electrical properties, mechanical robustness, environmental sustainability, and cost-effectiveness. However, its intrinsic limitations, including a gapless band structure that suppresses the Seebeck coefficient and extremely high thermal conductivity arising from the long mean free path (MFP) of phonons, restrict its energy-conversion efficiency.[13,31] Furthermore, the thermoelectric performance of graphene can vary significantly depending on the synthesis method,[11,43]

[a] *Department of Materials Science and Engineering, Korea University, Seoul 02841, Republic of Korea. E-mail: jeon39@korea.ac.kr*

[b] *Nano Hybrid Technology Research Center, Korea Electrotechnology Research Institute (KERI), Changwon, 51543, Republic of Korea. E-mail: mwchoi@keri.re.kr*

† These authors contributed equally to this work.

presenting additional challenges for optimization. To overcome these limitations, strategies such as nanostructuring,[44,45] doping,[46,47] grain-boundary tuning,[31–33,48] and defect engineering[13,49] have been explored to decouple and optimize the thermoelectric parameters of graphene. Despite significant research progress, the practical utilization of graphene in thermoelectric systems remains limited. These limitations arise from difficulties in establishing a temperature gradient across dimensions—particularly in the finite out-of-plane direction—due to its two-dimensional (2D) structure with a single atomic layer.[50] Additionally, graphene exhibits a low thermoelectric conversion efficiency (5.42×10^{-3} at 350 K),[13] even with the implementation of nanostructuring strategies.

As an alternative, a promising approach to harness the superior properties of graphene for thermoelectric applications is its selective use as a filler in hybrid composite systems. Hybridization with graphene allows the thermoelectric parameters to be decoupled by leveraging its ability to increase electrical conductivity,[51,52] reduce thermal conductivity via phonon scattering,[12,53] and induce energy-filtering effects.[54] The enhancement of thermoelectric performance through graphene hybridization can be optimized by initially nanostructuring the thermoelectric material to increase its specific surface area, which facilitates graphene integration and interaction at the nanoscale. Notably, graphene hybridization with nanostructured thermoelectric materials has achieved significant

improvements in zT values. For example, researchers improved the thermoelectric performance by incorporating partially reduced graphene oxide (rGO) into nanostructured TiO_2.[55] In this study, rGO flakes were strategically distributed near grain boundaries and defect sites within the TiO_2 matrix, resulting in a synergistic effect. The highly conductive pathways provided by rGO, while activating phonon scattering at hetero-interfaces, significantly reduced the thermal conductivity, causing a 3-fold improvement in the zT value at 325 K. This dual effect demonstrates the potential of graphene-based hybrid systems to overcome intrinsic limitations of conventional thermoelectric materials and achieve higher energy-conversion efficiencies.

While previous reviews[56,57] have explored the thermoelectric properties of graphene and graphene-based composites, a focused analysis of the role of graphene in nanostructured hybrid thermoelectric systems remains absent. This review aims to fill that gap by analyzing theoretical and experimental findings related to the thermoelectric properties of graphene, including its intrinsic limitations and optimization strategies. The review further explores the integration of graphene with one-dimensional (1D), 2D, and three-dimensional (3D) nanostructured thermoelectric materials, clarifying the underlying mechanisms that maximize the filler effect of graphene, such as efficient carrier transport, phonon scattering, and energy filtering (Fig. 1). Finally, we discuss the practical potential and
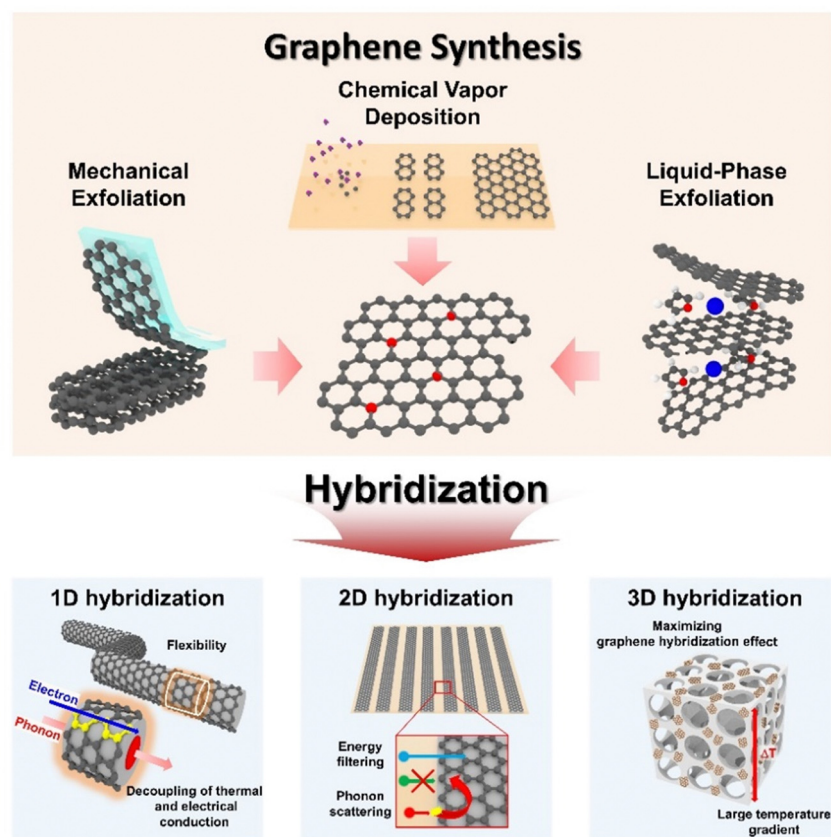

Fig. 1 Synthesis methods and hybridization strategies for utilizing graphene as a thermoelectric material.

future directions of graphene-based hybrid thermoelectric materials for energy-harvesting applications.

2. Thermoelectric properties of graphene

As mentioned in the Introduction, graphene exhibits exceptional electrical conductivity, mechanical flexibility, and high carrier mobility, making it a promising material for thermoelectric applications.[58–61] It is a gapless semiconductor with a linear dispersion relation, where charge carriers behave as massless Dirac fermions.[62] At the charge neutrality point (CNP), which is also known as the Dirac point, the density of states becomes zero, and graphene transitions between electron-like and hole-like behavior.[63] The electronic properties of graphene are governed by the relativistic Dirac equation rather than the non-relativistic Schrödinger equation, allowing ballistic transport over submicron distances.[57,64] These unique electrical properties and band structure of graphene originate from the delocalized π-electron network formed by p orbitals in its honeycomb lattice structure. However, its direct use in thermoelectric devices remains challenging because of its gapless electronic structure and exceptionally high thermal conductivity.[65,66] Therefore, various strategies, such as nanostructuring,[67] doping,[68] and composite approaches,[69] are actively being explored recently to enhance the thermoelectric performance of graphene.

Nanostructuring strategies have been widely utilized to modify the transport properties of electrons and phonons for enhancing the thermoelectric performance of conventional materials. These approaches have been extended to graphene, and researchers have reported significant theoretical and experimental improvements in its thermoelectric properties. For example, Nam et al. fabricated bilayer-graphene without nanostructuring to compare its experimentally measured Seebeck coefficient and thermoelectric power with calculated values based on the Mott relation.[70] Although the bandgap opening near the CNP under a back-gate voltage was expected to result in a Seebeck coefficient close to the theoretical prediction, the experimental values were significantly lower.

This discrepancy was attributed to large fluctuations in the disorder potential, which likely hindered the formation of a bandgap. In contrast, nanostructured graphene has exhibited significant improvements in thermoelectric performance. H. Sevincli et al. investigated graphene nanoribbons (GNRs) with zigzag edges and calculated their thermoelectric parameters.[44] The zigzag-edged graphene nanoribbons (ZGNRs) exhibited a high zT value of nearly 4, primarily owing to the suppressed phonon conductance at zigzag-edge defects. Additionally, the level of disorder within the ribbon was identified as a critical parameter for enhancing the thermoelectric performance of ZGNRs. These findings highlight the potential of nanostructuring for optimizing the thermoelectric properties of graphene—particularly through phonon-transport modulation.

To address the intrinsically low power factor of graphene, researchers have employed substrate engineering. Duan et al. constructed devices featuring single-layer graphene flakes on a hexagonal boron nitride (hBN) substrate (Fig. 2(a)).[71] This configuration significantly enhanced the thermoelectric performance compared with devices on SiO$_2$ substrates—particularly for active-cooling applications. By using the hBN substrate, the surface charge states and amount of impurities originating from the SiO$_2$ substrate were reduced, increasing the carrier mobility and reducing the number of electron–hole puddles, which increased the Seebeck coefficient. Fig. 2(b) shows the gate-voltage (V_g) dependence of the Seebeck coefficient in the temperature range of 77–290 K. When V_g was applied to modulate the carrier concentration in graphene, the device exhibited a positive Seebeck coefficient in the hole-doped regime and a negative Seebeck coefficient in the electron-doped regime, with the highest Seebeck coefficient observed near the CNP. This led to a maximum power factor times temperature value of 10.35 W m^{-1} K^{-1} at room temperature, which exceeds those of other 2D materials and even some conventional thermoelectric materials.

While the theoretical enhancement of thermoelectric performance through the nanostructuring of graphene and the fabrication of passive devices via substrate engineering have been demonstrated, the practical utilization of graphene in sustainable thermoelectric energy-harvesting systems requires further investigation. Specifically, it is crucial to explore the
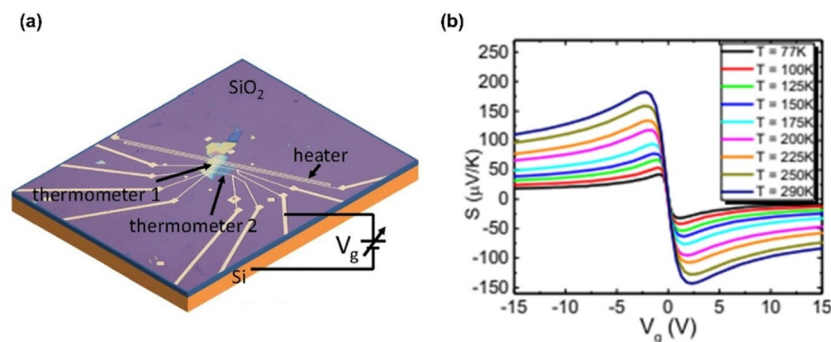

Fig. 2 (a) Schematic of graphene on an hBN device. (b) Back-gate dependence of S in the temperature range of 77–290 K. Reproduced with permission from ref. 71.

applicability of nanostructured graphene in energy-conversion devices, with experimental validation of its thermoelectric performance.

3. Synthesis methods for improving thermoelectric performance of graphene

The thermoelectric properties of graphene are significantly affected by the synthesis methods, as factors such as the number of graphene layers,[50,70] defect density,[13,31] and physical dimensions[44,45] can depend on the approach used. This section highlights experimental efforts aimed at enhancing the thermoelectric performance of graphene, focusing on strategies for nanostructuring and performance optimization. Two types of methods are discussed: bottom-up approaches, which are represented by chemical vapor deposition (CVD), and top-down approaches, which are represented by liquid-phase exfoliation.

3.1. CVD-based synthesis

For graphene synthesis, CVD benefits from nanostructuring strategies such as GNR synthesis,[72] grain-size control,[31] and grain-boundary engineering,[13] which selectively reduce thermal conductivity while maintaining high electrical conductivity. These strategies focus on enhancing phonon scattering at nanostructured interfaces in graphene, which reduces its intrinsically high thermal conductivity. For example, Li et al. synthesized GNRs through CVD, which successfully decoupled the electron and phonon transport.[45] As shown in Fig. 3(a), the device consists of a suspended GNR on a Ni substrate, which serves as a heater, sensor, and electrode. The synthesized GNR exhibited high electrical conductivity (5.66×10^6 S m^{-1} at 300 K) due to a low density of bulk defects. Additionally, it had a
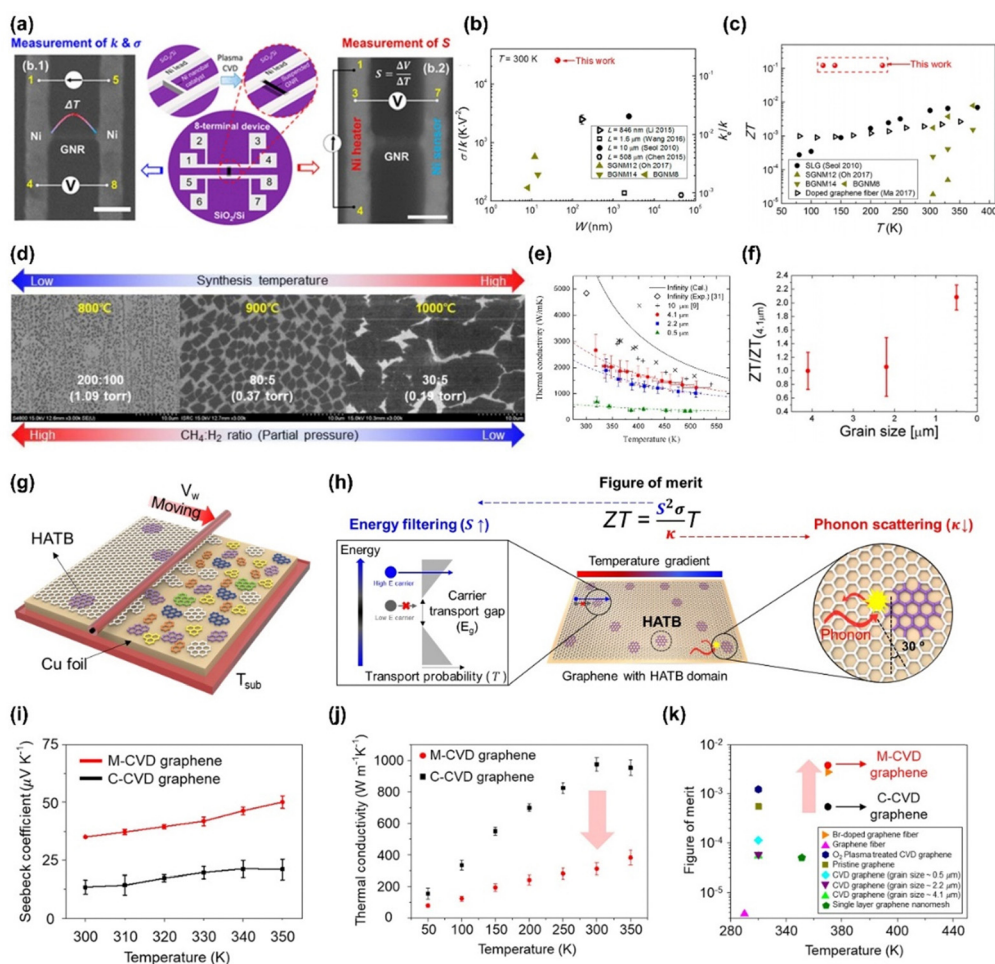

Fig. 3 (a) Test structure for the thermoelectric measurements of the GNR grown *via* CVD. (b) σ/k and k_e/k ratios of the suspended GNR compared with reference data. (c) zT value of the suspended GNR compared with reference data. Reproduced with permission from ref. 45. (d) Scanning electron microscopy (SEM) images of different nucleation densities in the initial growth state depending on the synthesis temperature and pressure. (e) Thermal conductivity as a function of temperature for different grain sizes. Reproduced with permission from ref. 31. (f) zT value of the graphene with the optimized grain size. Reproduced with permission from ref. 48. (g) Growth mechanism of MHW-CVD graphene. (h) Concept of increasing the graphene zT value in the MHW-CVD system. (i) Comparison between the Seebeck coefficients of M-CVD and C-CVD graphene. (j) Comparison between the thermal conductivities of M-CVD and C-CVD graphene. (k) zT values of M-CVD and C-CVD graphene compared with reference data. Reproduced with permission from ref. 13.

low thermal conductivity ($\sim$208 W m^{-1} K^{-1} at 300 K) resulting from the reduced phonon MFP and quasi-ballistic effects originating from its nanoscale dimensions. This combination led to a record-high electrical-to-thermal conductivity ratio (Fig. 3(b)). The quarter-micron lengths of GNR effectively reduced the lattice thermal conductivity, while the electrical conductivity remained relatively unaffected by the GNR length, as the phonon MFP ($\sim$282 nm) was significantly longer than the electron MFP ($\sim$50 nm). Furthermore, the bandgap opening in the nanostructured GNRs with quarter-micron lengths and low defect density resulted in a high Seebeck coefficient of 132.8 μV K^{-1} and high zT values of up to $\sim$0.1 at 220 K (Fig. 3(c)). These findings highlight that the size effect of graphene plays a crucial role in increasing the thermoelectric energy conversion efficiency, emphasizing the importance of precise control over length and dimensions during CVD synthesis.

Another strategy for enhancing phonon scattering in graphene is grain-size reduction. By controlling the conditions during the CVD process for graphene synthesis, such as the operating pressure, temperature, heating-/cooling-time intervals, and precursor-gas concentration ratios, the average grain size of graphene is systematically controlled (Fig. 3(d)).[31] As shown in Fig. 3(e), as the average grain size is reduced, the thermal conductivity tends to decrease, which results from the narrowing of the phonon dispersive range, limiting the contribution of long-wavelength phonons. For graphene with small grain sizes of 4.1 and 2.2 μm, the grain-size reduction narrows the phonon dispersive range, restricting the contribution of long-wavelength phonons and reducing the thermal conductivity. When the grain size is reduced to 500 nm, it becomes smaller than the phonon MFP of graphene, further reducing the thermal conductivity (340 W m^{-1} K^{-1}). A subsequent study indicated that this reduction in grain size is more effective than reducing the power factor for reducing the thermal conductivity (Fig. 3(f)).[48] Compared with a grain size of 4.1 μm, reductions to 2.2 and 0.5 μm resulted in electron MFP reductions of 23.3% and 49.8%, respectively, while the phonon MFPs decreased more substantially—by 24.5% and 68%, respectively. Accordingly, the highest thermoelectric zT value was achieved at a grain size of 0.5 μm, which was attributed to the effective phonon-boundary scattering. This indicates that controlling the grain size during CVD synthesis can increase the zT value.

Recent advancements in CVD have allowed more precise control over defects in graphene during its growth process. In particular, the mobile hot-wire CVD (MHW-CVD) system offers localized and sequential thermal treatment, allowing more refined control over graphene crystal growth compared with conventional CVD systems, which supply thermal energy globally.[13,38,73–75] This system enables the synthesis of highly oriented graphene with only two crystal orientations, separated by high-angle tilt boundaries (HATBs) with a misorientation angle of approximately 30°. These HATBs significantly affect the thermoelectric properties of graphene.[13] The strategy for enhancing the thermoelectric performance of graphene involves the formation of HATB domains that induce both energy filtering

and phonon scattering. In crystallographically misaligned graphene, a charge-carrier transport gap (E_g) is formed at grain boundaries. As the misalignment angle increases, E_g increases. Additionally, phonon scattering is enhanced in regions with a higher degree of misalignment owing to disordered structures at the interfaces between neighboring graphene grains. Normally, graphene exhibits a zero bandgap and a low Seebeck coefficient, as observed for C-CVD graphene (conventional CVD-grown graphene) in Fig. 3(i). However, in M-CVD (MHW-CVD) graphene, the substantial E_g created at the HATB domains provides an energy-filtering function that selectively blocks low-energy carriers corresponding to E_g. Thus, M-CVD graphene is expected to have a relatively high Seebeck coefficient due to the selective transport of charge carriers. The Seebeck coefficient of M-CVD graphene is 50.1 μV K^{-1} at 350 K, representing a 138% increase compared with that of C-CVD graphene. As shown in Fig. 3(j), HATB domains also reduce the thermal conductivity of graphene. The thermal conductivity of M-CVD graphene at 350 K is approximately 382 W m^{-1} K^{-1}, which is significantly lower than that of C-CVD graphene, indicating an increase in phonon scattering at the HATB domains. Fig. 3(k) shows the thermoelectric zT values for M-CVD and C-CVD graphene, which are derived from the experimental power factor and thermal conductivity data, along with other graphene-based thermoelectric materials. M-CVD graphene exhibits a maximum zT value of 3.78 $\times$ 10^{-3} at 350 K, which is nearly 7 times higher than that of C-CVD graphene. This approach can be used to enhance thermoelectric properties by simultaneously tuning grain boundaries and inducing nanostructuring effects through modifications in the CVD growth parameters, without the need for specific post-growth nanostructuring processes.

3.2. Liquid-phase exfoliation

While bottom-up CVD-based synthesis and nanostructuring strategies effectively decouple thermoelectric parameters (Seebeck coefficient, electrical conductivity, and thermal conductivity) to improve the thermoelectric performance, they face challenges with regard to scalability and controllability for practical applications. To address these limitations, liquid-phase exfoliation of graphite and their assembly have been developed, enabling large-scale production and precise control of synthesis conditions. Graphene produced via exfoliation not only benefits from these scalable and controllable processes but also exhibits lower thermal conductivity than CVD-derived graphene. This section explores liquid-phase graphene exfoliation methods, strategies for enhancing thermoelectric performance, factors influencing thermoelectric properties, and thermoelectric applications of graphene.

In top-down methods, minimizing defects during the exfoliation process is crucial for preserving the electrical properties of graphene flakes when they are assembled into films.[76] The most common technique for producing graphene flakes is the modified Hummers' method, which generates graphene oxide (GO).[77] Fig. 4(a) presents a schematic of the standard process for fabricating GO, which is followed by a post-treatment step to reduce GO into rGO. However, residual oxygenous groups
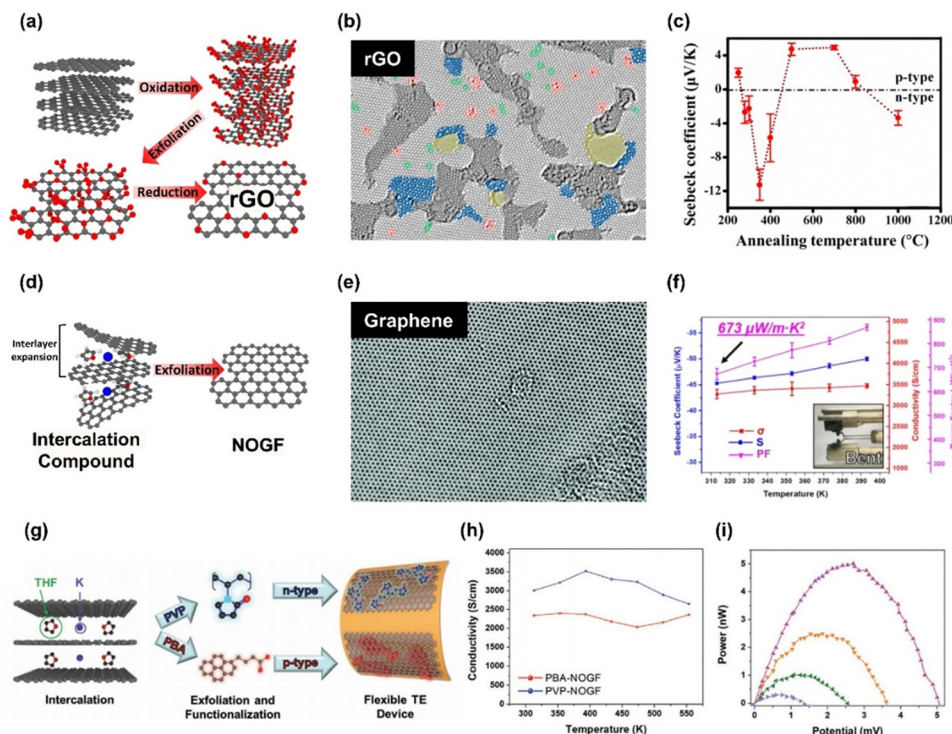
Fig. 4 (a) Schematic of the conventional rGO fabrication process. (b) Transmission electron microscopy (TEM) image of rGO. Reproduced with permission from ref. 78. (c) Seebeck coefficient of graphene as the function of the annealing temperature. Reproduced with permission from ref. 80. (d) Schematic of the NOGF fabrication process. (e) TEM image of graphene. (f) Electrical conductivity (σ), Seebeck coefficient (S), and power factor of the NOGF-based flexible thin films. Reproduced with permission from ref. 10. (g) Schematic of the experimental process for fabricating complementary p- and n-type graphene films by varying the surfactant during exfoliation. (h) Electrical conductivity of NOGFs as a function of the temperature. (i) Power output as a function of the potential at different temperatures. Reproduced with permission from ref. 11.

and defects remain in the basal plane of rGO flakes even after the intense chemical process at an extremely high temperature (Fig. 4(b)).[78] These oxidation-induced defects significantly degrade the thermoelectric performance of graphene, necessitating strategies to mitigate them for thermoelectric applications. Hu et al.[79] systematically investigated the impact of the reduction temperature on GO synthesized via Hummers' method, varying the reduction temperature from 500 to 3300 K.[79] Their study revealed that as the reduction temperature increased, the degree of oxidation decreased, leading to the restoration of crystallinity and a substantial increase in the thermoelectric power factor, which reached ~ 54.5 μW cm^{-1} K^{-2} at 3300 K. Raman spectroscopy supported these findings: a notable reduction in the D-to-G peak intensity ratio (I_D/I_G) from 1.11 to 0.08 was observed when the reduction temperature was increased from 1000 to 3300 K. Additionally, in contrast to GO reduced at 1000 K, the sample reduced at 3300 K exhibited a sharp 2D peak, indicating a more graphitic structure. The restoration of crystallinity at 3300 K resulted in a significant increase in its electrical conductivity, which reached approximately 4000 S cm^{-1} at 3000 K. Moreover, the increased Seebeck coefficient (~ 150 μV K^{-1} at 1200 K) was attributed to the suppression of low-energy hole transport and controlled electron scattering. Furthermore, addressing oxidation-related defects is critical owing to their impact on the doping behavior of graphene. As illustrated in

Fig. 4(c), the doping type of graphene can be tuned through annealing and selective functional group removal. However, rGO typically exhibits weak p-type thermoelectric behavior at room temperature.[80] To address the fundamental challenges associated with the intrinsic properties of rGO, it is essential to develop fabrication methods that preserve the high structural quality while enabling scalable production of graphene flakes. Consequently, the need for low-oxidation graphene from topdown methods has drawn attention to synthesis techniques based on graphite intercalation compounds (GICs).[81] Among the studies using GIC synthesis, flexible thermoelectric films produced from non-oxidized graphene flakes (NOGFs) were introduced. Fig. 4(d) presents schematics of the NOGF fabrication process, which contains before and after stage of expansion through intercalation. The resultant graphene was obtained via simple immersion method of graphite in potassium naphthalenide and tetrahydrofuran (THF) followed by mild sonication to form high-quality, large-scale flakes (Fig. 4(e)). The conductive film composed of NOGFs exhibits exceptional thermoelectric performance, achieving a room-temperature power factor of 673 μW m^{-1} K^{-2} (Fig. 4(f)).[10] This impressive result is attributed to its high electrical conductivity of 3280 S cm^{-1} and Seebeck coefficient of -45.3 μV K^{-1}, both of which originate from the minimal oxidation of the basal plane. Additionally, the films exhibit excellent mechanical stability, with <3%

reduction in electrical conductivity at a bending radius of 1 mm and stability after >1000 bending cycles.

In a follow-up study, the separation of doping types in NOGFs was investigated by varying the surfactants used during processing. Fig. 4(g) presents the experimental approach, which was based on previous research (Fig. 4(d)), and highlights the two distinct doping types observed in the resulting TE devices.[11] The process begins with the synthesis of a GIC by immersing raw graphite in a potassium naphthalenide solution, followed by gentle bath sonication for 30 min in DMSO with either polyvinylpyrrolidone (PVP) or pyrenebutyric acid (PBA) as a surfactant. By changing the adsorbed surfactant during the intercalation–exfoliation process (PVP for n-type, PBA for p-type), both extremely high electrical conductivity and high Seebeck coefficients of complementary n-type and p-type graphene can be achieved. Fig. 4(h) compares the in-plane thermoelectric properties of PVP-NOGF and PBA-NOGF films. Near room temperature (313 K), the PBA-NOGF film exhibits lower electrical conductivity (2330 S cm^{-1}) than the PVP-NOGF film (3010 S cm^{-1}), but both have relatively stable electrical conductivity across the temperature range. The power factor of the PBA-NOGF film (655 μW m^{-1} K^{-2}) is similar to that of the PVP-NOGF film (621 μW m^{-1} K^{-2}) under the same conditions. The power as a function of potential is presented in Fig. 4(i), showing the expected parabolic shape, with the height increasing as the temperature increases. The peak power output at 250 °C was 5.0 nW at 2.7 mV. The results of the study deviate from commonly used synthesis methods; rather, the researchers focused on enhancing the intrinsic thermoelectric properties of graphene. Additionally, distinct doping of graphene was achieved by adjusting the film's process variables, without additional post-treatment.

4. Graphene hybridization with thermoelectric materials for practical utilization

In the previous section, strategies for enhancing the thermoelectric performance of graphene through nanostructuring and synthesis were introduced, and key factors for using graphene as a thermoelectric material were discussed. However, using graphene alone as a thermoelectric material presents several challenges. Specifically, graphene inherently exhibits extremely high thermal conductivity and a near-zero bandgap, leading to a low Seebeck coefficient and consequently low thermoelectric conversion efficiency.[57] Although nanostructuring graphene to create a bandgap has been explored, the required nanoscale dimensions make practical application of graphene in thermoelectric devices difficult.[82] The hybridization strategy of using graphene as a filler in thermoelectric materials holds significant potential for addressing these limitations and enabling practical applications of graphene-based thermoelectric devices.[83] When used as a filler, graphene forms heterojunction networks that enhance high-energy electron filtering, increasing the Seebeck coefficient. In thermoelectric applications

using graphene as a filler to maximize the energy-filtering effect, inorganic semiconductors are primarily employed for not only their intrinsically high thermoelectric performance but also their moderate bandgap, which provides an optimal energy barrier with graphene.[82] Fundamentally, materials with either no bandgap (e.g., metals) exhibit a low Seebeck coefficient, while those with excessively large bandgaps (e.g., insulators) suffer from poor electrical conductivity.[82] However, graphene–inorganic semiconductor heterostructures exhibited an increased Seebeck coefficient without a significant reduction in electrical conductivity. For instance, Li et al. introduced a 3D graphene heterointerface that exhibited band bending into the Cu$_{2-x}$S matrix. The heterostructure was fabricated with a Cu$_{2-x}$S matrix, which typically has a bandgap of 1.6–2.2 eV, resulting in a ~50% increase in the power factor at 600 K compared with pristine Cu$_{2-x}$S.[84] Similarly, Jiang et al. fabricated an rGO/Bi$_2$Te$_3$ heterojunction network structure, which exhibited a 31% enhancement in the zT value compared with pure Bi$_2$Te$_3$.[85] Hybridization with Bi$_2$Te$_3$, which generally has a bandgap of ~0.4 eV, confirmed the energy-filtering effect. Generally, the enhancement of the Seebeck coefficient via the energy-filtering effect has been observed when the potential energy barrier exceeds approximately 0.3 eV.[86] In support of this concept, experimental studies have demonstrated a remarkable enhancement in thermoelectric performance through the hybridization of ZnO (bandgap of ~3 eV) with graphene quantum dots (GQDs) possessing a controlled bandgap of ~3.2 eV.[12] Furthermore, nanostructured graphene interfaced within a matrix increases the degree of phonon scattering at the heterointerface, reducing the thermal conductivity, which significantly improves the overall thermoelectric performance. As the size of the matrix is correlated with the practical dimensions of thermoelectric devices, nanostructured graphene can be achieved through the realization of graphene as a functional component in actual thermoelectric devices. Therefore, this section introduces strategies for hybridizing graphene as a filler with thermoelectric materials in various 1D, 2D, and 3D forms or structures to surpass the performance of conventional single thermoelectric materials. This approach facilitates the development of thermoelectric metamaterials by combining nanostructuring and graphene hybridization to enhance thermoelectric performance.

4.1. Hybridization of graphene with 1D materials

The hybridization of graphene with 1D materials has demonstrated the ability to independently control electrical and thermal properties, suggesting that graphene is a promising thermoelectric material. Lee et al. aimed to enhance the thermoelectric performance of a composite by independently controlling the electrical and thermal properties through the encapsulation of Si and SiO$_2$ nanowires with graphene (Fig. 5(a)).[87] In the composite of graphene with Si and SiO$_2$ nanowires, the graphene shell significantly increases the electrical conductivity (Fig. 5(b)), while the nanowire core regulates the thermal conductivity (Fig. 5(c)). This hybridization directs phonons predominantly through the core owing to its larger cross-sectional area, which makes it more effective for conducting thermal energy. Meanwhile, the graphene shell, despite its relatively small cross-sectional area, exhibits
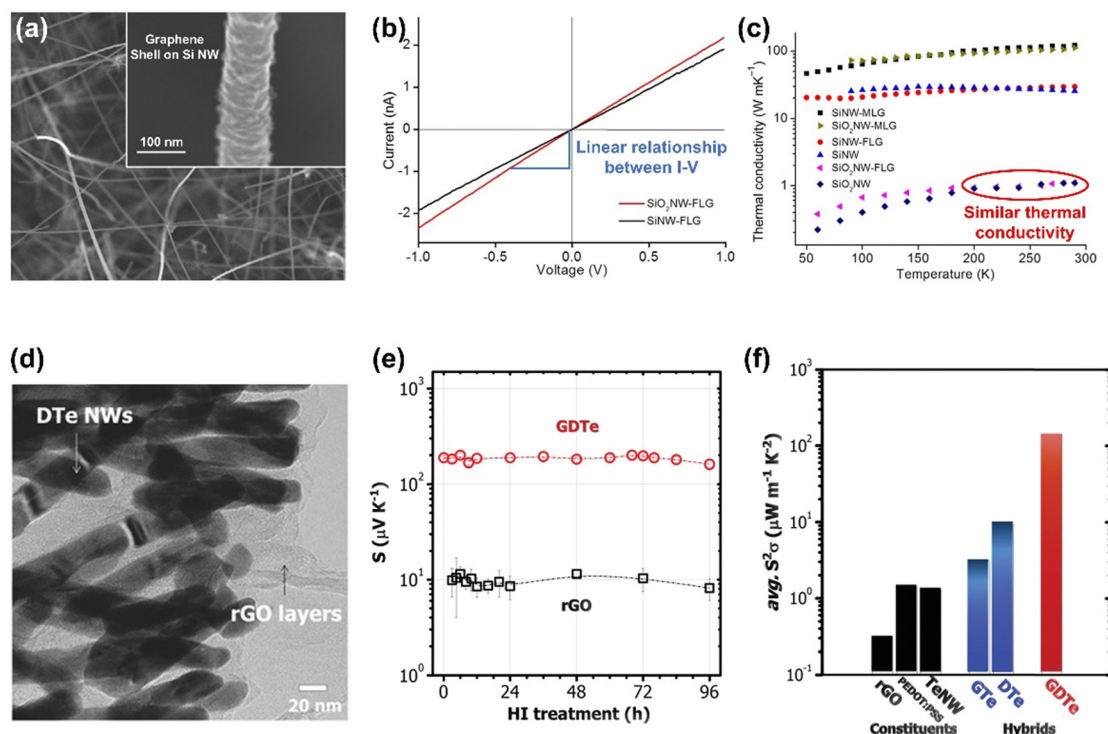
Fig. 5 Hybridization of graphene with 1D materials for enhancing the thermoelectric performance. (a) SEM images of Si nanowire–graphitic shell composites. (b) Current–voltage (I–V) curves of Si/SiO$_2$ nanowire–graphitic shell composites. (c) Dependence of the thermal conductivity on the thickness of the graphitic shell. Reproduced with permission from ref. 87. (d) TEM images of DTe nanowires and rGO hybridization. (e) Comparison of the Seebeck coefficient between GDTe nanowires and rGO. (f) Comparison of power factors between single constituents and hybrids. Reproduced with permission from ref. 88.

outstanding electrical conductivity owing to its superior charge-carrier mobility. Thus, the improvement in electrical conductivity does not lead to a corresponding increase in thermal conductivity, increasing the thermoelectric zT.

Furthermore, Choi *et al.* utilized a ternary composite consisting of graphene, a polymer (PEDOT:PSS), and Te nanowires (TeNWs) to improve thermoelectric performance (Fig. 5(d)).[88] The hybridization of graphene with TeNWs increased both the electrical conductivity and the Seebeck coefficient. The high charge-carrier mobility of graphene, combined with the flexibility of the polymer, optimized the electrical conduction pathways and efficiently filtered out low-energy charge carriers, allowing only high-energy carriers to contribute to electrical transport. In this study, a double carrier-filtering effect was induced at the heterojunctions, enhancing the thermoelectric properties without significantly increasing the thermal conductivity. The multiple interfaces formed by the combination of graphene, TeNWs, and PEDOT:PSS functioned as energy barriers for low-energy charge carriers, facilitating the selective transport of high-energy carriers. This selective filtering mechanism led to concurrent improvements in electrical conductivity and the Seebeck coefficient (Fig. 5(e)), increasing the power factor (Fig. 5(f)). These findings emphasize the significance of optimizing heterojunction characteristics to balance electrical conductivity and thermal conductivity in thermoelectric materials. The ability to precisely control carrier-transport properties

through heterostructure design offers a promising route to further increase zT values.

4.2. Hybridization of graphene with 2D materials

The hybridization strategy of encapsulating 1D nanowires with graphene offers advantages in decoupling electrical and thermal conduction paths. However, it faces limitations due to insufficient active heterojunction sites for high-energy electron filtering, which restricts the Seebeck coefficient. Additionally, the small grain boundaries in 1D structures reduce the probability of phonon scattering. To overcome these challenges, researchers have explored the hybridization of graphene with 2D sheet-like matrices. The integration of graphene with 2D structures is enabled by enhanced grain-boundary engineering and bandgap tuning, which facilitates both phonon scattering and energy filtering, addressing the limitations of 1D hybridization.[89,90]

Oh *et al.* fabricated a heterojunction network that combined GNRs with monolayer molybdenum disulfide (MoS$_2$) to improve the thermoelectric performance (Fig. 6(a)).[91] The heterojunction was designed to leverage the distinctive properties of each component: GNRs, known for their high electrical conductivity and band structure modulation capabilities, were paired with MoS$_2$, which has semiconducting properties[92] and a direct bandgap of approximately 1.8 eV. The GNR/MoS$_2$ heterojunction network structure provided significant advantages for thermoelectric
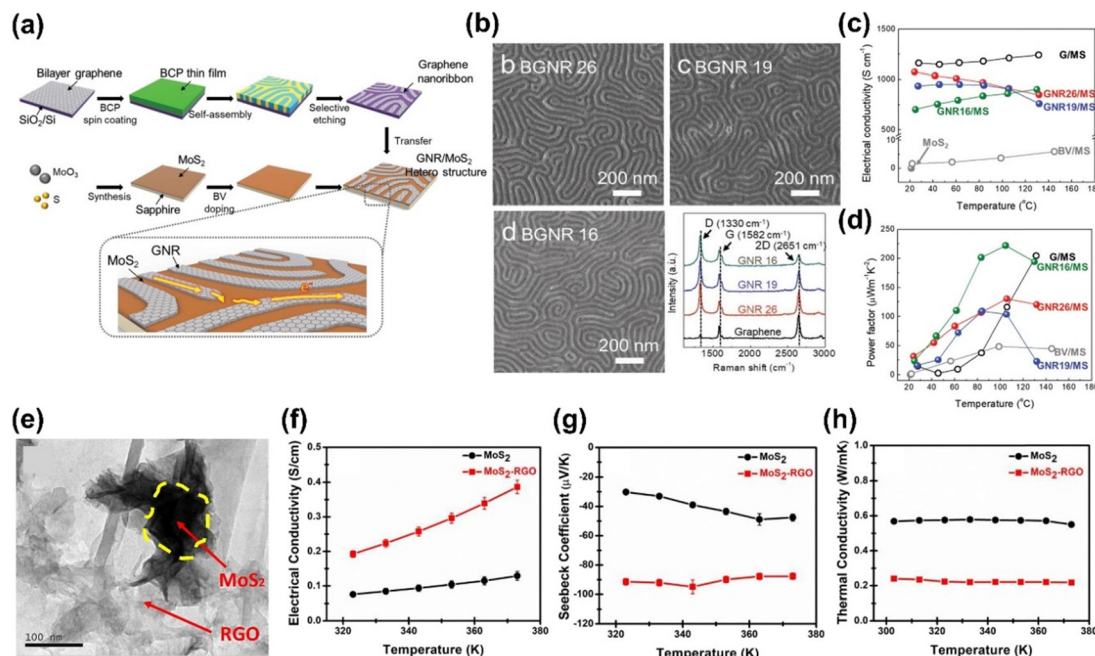
Fig. 6 Enhancing phonon scattering and energy filtering in the hybridization of graphene with 2D materials. (a) Schematic of the GNR–MoS$_2$ heterojunction. (b) SEM images of GNR patterns with varying linewidths. (c) Electrical conductivity and (d) power factor of graphene hybridized with MoS$_2$. Reproduced with permission from ref. 91. (e) TEM images of MoS$_2$–RGO hybridization. Comparison of the (f) electrical conductivity, (g) Seebeck coefficient, and (h) Thermal conductivity between single MoS$_2$ and hybridized MoS$_2$–RGO. Reproduced with permission from ref. 93.

performance owing to its unique ability to form vertical carrier paths through a van der Waals interface. This structure allowed charge carriers to traverse between GNRs and MoS$_2$ through the heterojunction, maximizing the interface's contribution to the overall electrical and thermoelectric properties. GNRs functioned as efficient conductive channels, while the MoS$_2$ layers increased the Seebeck coefficient by providing additional bandgap tuning and acting as energy barriers for selective carrier transport. The introduction of a 1-nm-thick layer of benzyl viologen (BV) at the heterojunction further improved carrier transport by serving as a thin tunneling barrier and modulating the Fermi level of MoS$_2$. By controlling the linewidth of the GNRs, the researchers demonstrated that it was possible to optimize the band structure and consequently the thermoelectric performance of the heterojunction network (Fig. 6(b)). GNRs with narrower linewidths exhibited higher quantum confinement, leading to an increased bandgap. This change increased the Seebeck coefficient and reduced the thermal conductivity. The GNR/MoS$_2$ heterojunction network achieved an electrical conductivity of up to 1163 S cm^{-1} (Fig. 6(c)) and a power factor of 222 μW m^{-1} K^{-2} (Fig. 6(d)), representing significant improvements over pristine MoS$_2$. The careful engineering of interfacial properties was key to the success of the heterojunction. By introducing the BV layer and tuning the GNR linewidth, the interfacial resistance was reduced, and band-to-band tunneling effects were enhanced, leading to more efficient charge transfer across the interface. This approach allowed optimization of the power factor without a corresponding increase in thermal conductivity, which is critical for

achieving a high thermoelectric zT. Moreover, the multiple interfaces and the introduced energy-filtering effects were crucial in improving both the electrical conductivity and the Seebeck coefficient while keeping the thermal conductivity low Gautam et $al.$ reported that the hybridization of MoS$_2$ with rGO (partially reduced graphene oxide) significantly improved the thermoelectric performance.[93] The primary challenge with MoS$_2$ as a thermoelectric material lies in its low electrical conductivity[94] despite its intrinsically low thermal conductivity. By forming a nanocomposite with rGO, they aimed to improve the thermoelectric zT by increasing the electrical conductivity, increasing the Seebeck coefficient, and reducing the thermal conductivity (Fig. 6(e)). The hybridization of rGO within the MoS$_2$ matrix provided multiple conductive pathways, reducing the interface barrier height and enhancing the scattering of phonons. This reduced the thermal conductivity while creating more effective conductive channels for electron transport, increasing the electrical conductivity. The synergistic interaction between MoS$_2$ and rGO was facilitated by their intimate contact, accelerating electron transfer across the nanocomposite. The presence of rGO effectively optimized the electron-transport properties of the MoS$_2$ matrix, resulting in a higher electrical conductivity, which was approximately 171% higher than that of pristine MoS$_2$ at room temperature (Fig. 6(f)). Moreover, the Seebeck coefficient of the MoS$_2$/rGO nanocomposite was significantly increased (Fig. 6(g)). This was partly due to the reduction of interface barriers, which allowed more efficient transfer of high-energy charge carriers, increasing the thermoelectric potential. Additionally, the thermal conductivity

was reduced through increased phonon scattering at the heterogeneous interfaces between MoS_2 and rGO. The lattice part of the thermal conductivity was reduced by 61%, contributing to the overall improvement in thermoelectric performance (Fig. 6(h)). These combined improvements led to an impressive 60-fold enhancement in the thermoelectric zT of the composite compared with pristine MoS_2.

4.3. Hybridization of graphene with 3D materials

The hybridization of graphene with 2D materials is enabled by enhanced phonon scattering and energy filtering, which can be further amplified by integrating graphene with 3D materials. Porous 3D structures provide significantly more active sites than 2D materials, maximizing the effects of phonon scattering and energy filtering.[56] Moreover, if nanostructured 3D matrices can be fabricated at the bulk scale, they can facilitate the practical implementation of graphene as a functional component in thermoelectric devices.

Tang et al. explored this approach by incorporating graphene into a copper sulfide ($Cu_{2-x}S$) matrix, which led to improved thermoelectric properties and thermal stability.[84] The integration was performed through a combination of mechanical alloying and spark plasma sintering, creating a graphene–$Cu_{2-x}S$ composite with a 3D graphene network (Fig. 7(a)). The inclusion of graphene had multiple beneficial effects. First, the graphene network contributed to Fermi-level pinning at the $Cu_{2-x}S$ interfaces (Fig. 7(b)), ensuring that only high-energy carriers contributed to electrical transport, which significantly increased the electrical conductivity of the composite (Fig. 7(c)). This energy-filtering effect allowed high-energy carriers to dominate electrical transport while scattering low-energy carriers, which increased the Seebeck coefficient. This selective carrier transport significantly increased the composite's power factor, which reached 1197 $\mu W\ m^{-1}\ K^{-2}$ at 873 K.

Additionally, the interfacial engineering introduced by the graphene network enhanced phonon scattering, significantly reducing the thermal conductivity of the composite (Fig. 7(d)). The presence of graphene at the grain boundaries and within the copper sulfide lattice disrupted the continuity of the lattice and introduced additional scattering centers for phonons, reducing the lattice thermal conductivity. The porous 3D graphene structure also suppressed grain growth during sintering, leading to a high density of grain boundaries, which further contributed to phonon scattering. This resulted in a thermal conductivity as low as 0.67 $W\ m^{-1}\ K^{-1}$ at 873 K, which was significantly lower than that of the pristine $Cu_{2-x}S$ (Fig. 7(e)). Overall, the high density of grain boundaries resulting from the hybridization of graphene with 3D $Cu_{2-x}S$ enhanced the energy filtering and phonon scattering, significantly increasing the thermoelectric zT, which reached 1.56 at 873 K—a value considerably higher than that of pristine $Cu_{2-x}S$ (Fig. 7(f)).

Graphene hybridization may be more effective when combined with the rational design of 3D nanostructured thermoelectric materials.[95,96] Kim et al. fabricated highly ordered and large-scale periodic 3D ZnO nanostructures via proximity-field nanopatterning (PnP), achieving a practical zT (~ 0.017 at 333 K and ~ 0.024 at 423 K) for pure ZnO. This performance was attributed to the significant reduction in thermal conductivity due to extensive phonon scattering at the numerous periodic nanostructured interfaces.[9] PnP—a 3D interference lithography-based nanofabrication method—has potential for the scalable production of nanostructured thermoelectric materials for device applications.[97–105] Furthermore, structural design for thermoelectric materials can enhance the thermoelectric performance without the need for doping. Integrating graphene into these optimized 3D nanostructures can further improve the thermoelectric performance.[12] For example, Choi et al. significantly improved the thermoelectric properties of
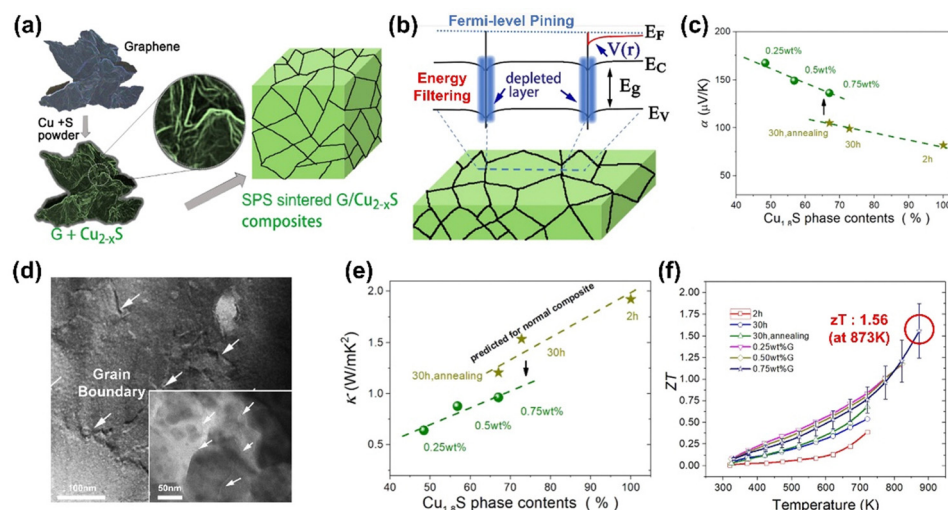

Fig. 7 Hybridization of graphene with 3D bulk materials for enhancing the thermoelectric performance. (a) Schematic of the fabrication process for graphene–$Cu_{2-x}S$. (b) Energy filtering in the depleted layer. (c) Seebeck coefficient as a function of the graphene concentration. (d) TEM images of graphene–$Cu_{2-x}S$ and the grain boundaries. (e) Thermal conductivity as a function of the graphene concentration. (f) Highest zT value of graphene–$Cu_{2-x}S$. Reproduced with permission from ref. 84.
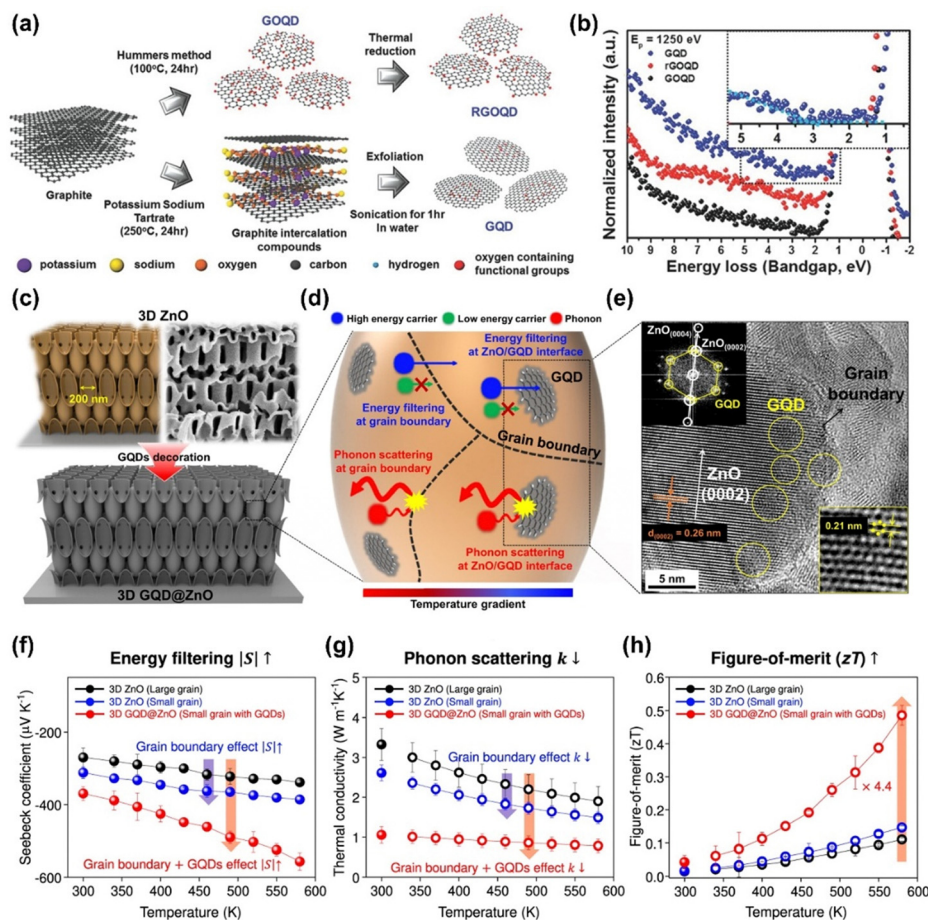
Fig. 8 Maximizing thermoelectric-performance enhancement through GQD interfacing in the nanostructured 3D matrix. (a) Schematic of the GQD fabrication process. (b) Bandgap differences between GQDs, rROQDs, and GOQDs. Reproduced with permission from ref. 106. (c) Field-emission SEM image and schematic of GQD-interfaced 3D ZnO (3D GQD@ZnO). (d) Sketch of phonon-scattering and energy-filtering effects at grain boundaries and GQD/ZnO interfaces. (e) TEM images of 3D GQD@ZnO (inset: high-resolution TEM image of 3D GQD@ZnO). (f)–(h) show the Seebeck coefficient, thermal conductivity, and zT of the 3D GQD@ZnO. Reproduced with permission from ref. 12.

ZnO through 3D nanostructuring and graphene hybridization.[12] The 3D continuous, highly ordered porous ZnO matrix provided abundant active sites for the attachment of graphene nanoflakes, which were called GQDs. High-quality GQDs were synthesized from GICs in a process that involved minimal oxidation (Fig. 8(a)).[106,107] The integration of low-oxidation GQDs into a 3D ZnO nanostructure led to significant enhancements in several key thermoelectric factors, such as the Seebeck coefficient, electrical conductivity, and thermal stability. The 5-nm GQD, with a distinct energy bandgap (~ 3.2 eV) (Fig. 8(b)), exhibited a larger bandgap than ZnO (~ 3 eV).[108] This difference suggests the potential formation of an interfacial energy barrier, depending on the valence-band maximum of ZnO and the highest occupied molecular orbital of the GQD. Specifically, the interfacing of GQDs with the porous ZnO matrix resulted in the formation of well-controlled interfacial energy barriers approximately 0.63 eV in height, which functioned as electron filters. These energy barriers selectively allowed only high-energy electrons to contribute to electrical conduction, while scattering lower-energy carriers (Fig. 8(c)). This selective electron filtering contributed to a substantial improvement of 74%

in the power factor compared with the pristine ZnO matrix, indicating the effectiveness of GQDs for enhancing thermoelectric performance (Fig. 8(f)). Moreover, the numerous heterogeneous interfaces between the GQDs and the ZnO matrix played a crucial role in inducing extensive phonon scattering (Fig. 8(d)), which significantly reduced the thermal conductivity from 1.49 to 0.785 W m^{-1} K^{-1} (Fig. 8(g)). This reduction in thermal conductivity, combined with the improved electrical properties, contributed to an increased thermoelectric zT for the composite. The zT reached 0.486 at 580 K, setting a new benchmark for ZnO-based thermoelectric materials (Fig. 8(h)).

This research highlights the significant potential of utilizing nanosized graphene additives such as GQDs to fine-tune the electrical and thermal properties of thermoelectric materials. The combination of GQDs with a porous oxide matrix proved to be a viable strategy for improving the thermoelectric figure of merit by leveraging interface engineering and nanoscale material properties. The development of such hybrid materials not only provides a promising approach to address the limitations of traditional thermoelectric systems but also supports the

advancement of sustainable energy-harvesting technologies capable of converting waste heat into useful electrical energy.

5. Conclusions and outlook

Graphene is promising for thermoelectric applications because of its high electrical conductivity, mechanical strength, and flexibility. However, its intrinsic limitations, such as its high thermal conductivity and a near-zero bandgap, significantly restrict its thermoelectric performance. Specifically, the high thermal conductivity suppresses the temperature gradient essential for thermoelectric energy conversion, while the near-zero bandgap results in a low Seebeck coefficient, limiting the energy-conversion efficiency. Over the past decade, various strategies have been explored to address these challenges, including nanostructuring, grain-boundary engineering, chemical doping, and defect modulation. While these approaches have yielded improvements, they remain insufficient for realizing highly efficient thermoelectric performance in graphene-based systems.

A promising strategy to overcome these limitations lies in the hybridization of graphene with thermoelectric matrices. Graphene, when employed as a filler, offers a unique advantage in decoupling the three critical thermoelectric parameters—electrical conductivity, Seebeck coefficient, and thermal conductivity—by facilitating charge-carrier transport, phonon scattering, and energy filtering. For example, 2D transition-metal dichalcogenides such as MoS_2,[93] Cu_2Te,[109] and $PbSe$[110] can effectively modulate electron and phonon transport when integrated with graphene, enhancing thermoelectric performance. Additionally, polymer-based hybridization with materials such as PEDOT:PSS[111] and PANI[112] offers a lightweight, flexible, and cost-effective approach for fabricating scalable thermoelectric composites. Finally, the integration of graphene with oxide-based thermoelectric materials such as ZnO,[12] Al-doped ZnO[51] and lanthanum strontium titanium oxide,[113] which are highly compatible with semiconductor processing, can significantly improve thermoelectric performance while maintaining practical manufacturability. The synergistic hybridization effect is further amplified when graphene is integrated with nanostructured or porous thermoelectric matrices. These structures increase the specific surface area, creating active sites for graphene interaction and improving electrical pathways while suppressing thermal conductivity through enhanced phonon scattering at the heterointerfaces. Fig. 9 shows the peak zT values in various temperature ranges before and after graphene hybridization.[12,51,52,55,113–119] Graphene hybridization not only improves the performance of existing thermoelectric materials but also induces hybridization effects across the entire temperature range owing to the high thermal stability of graphene. This observation highlights the versatility of graphene as a thermoelectric filler capable of enhancing performance under both low- and high-temperature conditions. Furthermore, the integration of graphene into thermoelectric devices addresses many limitations of traditional thermoelectric materials and systems. Hybrid graphene-based thermoelectric materials
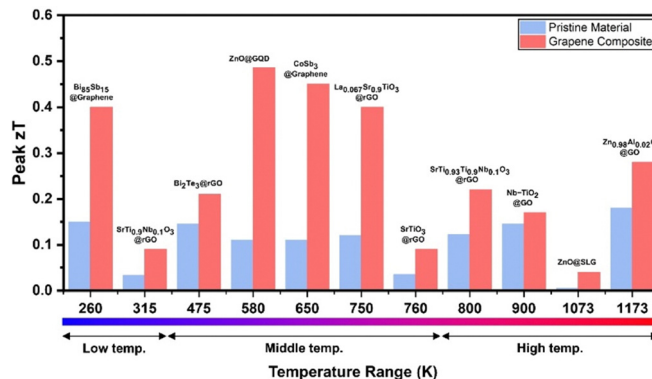

Fig. 9 Peak ZT values of pristine materials and graphene composites: (1) $Bi_{85}Sb_{15}$/graphene,[114] (2) $SrTi_{0.9}Nb_{0.1}O_3$/rGO,[115] (3) Bi_2Te_3/rGO,[116] (4) ZnO/GQD,[12] (5) $CoSb_3$/graphene,[117] (6) $La_{0.067}Sr_{0.9}TiO_3$/rGO,[113] (7) $SrTiO_3$/rGO,[52] (8) $Sr_{0.93}Ti_{0.90}Nb_{0.10}O_3$/rGO,[118] (9) $Nb–TiO_2$/GO,[55] (10) ZnO/SLG,[119] and (11) $Zn_{0.98}Al_{0.02}O$/GO.[51]

exploiting the properties of graphene, such as non-toxicity, abundance, and cost-efficiency, play a pivotal role in sustainably advancing the development of energy-harvesting systems across diverse applications. Such advancements have significant implications for the development of eco-friendly and sustainable energy-harvesting technologies.

To accelerate the commercialization of graphene-based thermoelectric materials, several critical challenges must be addressed. First, the exploration of mass-production technologies for high-quality graphene using low-cost and scalable methods is essential.[120] Methods such as CVD and solution-based exfoliation should be refined to produce graphene with controllable thickness and quality at an industrial scale. Second, future research should focus on developing robust and scalable synthesis processes for hybrid thermoelectric materials that effectively incorporate graphene while maintaining structural and functional integrity. In addition, further investigation into the mechanisms underlying graphene hybridization effects, such as phonon–electron interactions, energy filtering phenomena, and interfacial thermal resistance, will provide valuable insights for optimizing material design. Multiscale modeling and advanced characterization techniques should be employed to elucidate the structure–property–performance relationships of graphene-based thermoelectric materials. Another priority is the exploration of thermoelectric device technology tailored for graphene-based hybrid materials, *e.g.*, designing and optimizing device architectures to maximize the energy-conversion efficiency of graphene-integrated systems.

In conclusion, graphene-based thermoelectric materials offer immense potential to revolutionize sustainable energy solutions. With the advancement of mass-production technologies, improvements in hybrid material design, and the development of scalable thermoelectric devices, graphene can play a pivotal role in next-generation energy-harvesting systems. Such efforts will be crucial in bridging the gap between fundamental research and real-world deployment, enabling the widespread use of graphene-based thermoelectric technologies in sustainable energy systems and beyond.

Author contributions

J. K., H. C., G. B., and M. C. wrote the manuscript. M. C. and S. J. supervised the study. All the authors approved the final version of the manuscript.

Data availability

No primary research results, software, or code have been included and no new data were generated or analyzed as part of this review.

Conflicts of interest

There are no conflicts to declare.

Acknowledgements

Notes and references

1 P. N. Navya and H. K. Daima, *Nano Convergence*, 2016, **3**, 1.
2 J. J. Yoo, G. Seo, M. R. Chua, T. G. Park, Y. Lu, F. Rotermund, Y.-K. Kim, C. S. Moon, N. J. Jeon, J.-P. Correa-Baena, V. Bulović, S. S. Shin, M. G. Bawendi and J. Seo, *Nature*, 2021, **590**, 587–593.
3 W. J. Jang, E. H. Kim, J. H. Cho, D. Lee and S. Y. Kim, *Adv. Sci.*, 2024, **11**, 2406657.
4 H. Kim, S. Yun, K. Kim, W. Kim, J. Ryu, H. G. Nam, S. M. Han, S. Jeon and S. Hong, *Nano Energy*, 2020, **78**, 105259.
5 S. Chen, J. Luo, X. Wang, Q. Li, L. Zhou, C. Liu and C. Feng, *Sci. Rep.*, 2020, **10**, 8895.
6 S. Niu and Z. L. Wang, *Nano Energy*, 2015, **14**, 161–192.
7 M. Alzgool, M. Mousavi, B. Davaji and S. Towfighian, *Nano Energy*, 2022, **103**, 107758.
8 B. Meng, W. Tang, X. Zhang, M. Han, W. Liu and H. Zhang, *Nano Energy*, 2013, **2**, 1101–1106.
9 K. Kim, J. Park, S. Hong, S. H. Park, S. G. Jeon, C. Ahn, J. Y. Song and S. Jeon, *Nanoscale*, 2018, **10**, 3046–3052.
10 T. G. Novak, J. Kim, J. Kim, H. Shin, A. P. Tiwari, J. Y. Song and S. Jeon, *2D Mater.*, 2019, **6**, 045019.
11 T. G. Novak, J. Kim, J. Kim, A. P. Tiwari, H. Shin, J. Y. Song and S. Jeon, *Adv. Funct. Mater.*, 2020, **30**, 2001760.
12 M. Choi, J. An, H. Lee, H. Jang, J. H. Park, D. Cho, J. Y. Song, S. M. Kim, M.-W. Oh and H. Shin, *Nat. Commun.*, 1996, **15**, 2024.
13 M. Choi, T. G. Novak, J. Byen, H. Lee, J. Baek, S. Hong, K. Kim, J. Song, H. Shin and S. Jeon, *ACS Appl. Mater. Interfaces*, 2021, **13**, 24304–24313.
14 M. Choi, G. Lee, Y. L. Lee, H. Lee, J. H. Yang, H. Jang, H. Han, M. Kang, S. Yoo and A. R. Jang, *InfoMat*, 2024, e12626.
15 S. Boccardi, F. Ciampa and M. Meo, *Smart Mater. Struct.*, 2019, **28**, 105057.
16 A. Sarris, B. Bhatti and F. Ciampa, *J. Intell. Mater. Syst. Struct.*, 2022, **33**, 1602–1612.
17 J. Mativo and K. Hallinan, *Energy Harvesting Syst.*, 2019, **4**, 87–105.
18 R. Stobart, M. A. Wijewardane and Z. Yang, *Appl. Therm. Eng.*, 2017, **112**, 1433–1444.
19 X. Li, C. Xie, S. Quan, Y. Shi and Z. Tang, *IEEE Access*, 2019, **7**, 72143–72157.
20 D. Luo, Z. Wu, Y. Yan, D. Ji, Z. Cheng, R. Wang, Y. Li and X. Yang, *Appl. Therm. Eng.*, 2023, **227**, 120360.
21 S. Khan, J. Kim, K. Roh, G. Park and W. Kim, *Nano Energy*, 2021, **87**, 106180.
22 H. Park, D. Lee, D. Kim, H. Cho, Y. Eom, J. Hwang, H. Kim, J. Kim, S. Han and W. Kim, *J. Phys. D: Appl. Phys.*, 2018, **51**, 365501.
23 Y. Liu, X. Wang, S. Hou, Z. Wu, J. Wang, J. Mao, Q. Zhang, Z. Liu and F. Cao, *Nat. Commun.*, 2023, **14**, 3058.
24 D. Zhao, X. Lu, T. Fan, Y. S. Wu, L. Lou, Q. Wang, J. Fan and R. Yang, *Appl. Energy*, 2018, **218**, 282–291.
25 B. Shang, Y. Ma, R. Hu, C. Yuan, J. Hu and X. Luo, *Appl. Therm. Eng.*, 2017, **118**, 593–599.
26 J. Smith, R. Singh, M. Hinterberger and M. Mochizuki, *Int. J. Therm. Sci.*, 2018, **134**, 517–529.
27 C. Xiao, Z. Li, K. Li, P. Huang and Y. Xie, *Acc. Chem. Res.*, 2014, **47**, 1287–1295.
28 D. D. Fan, H. J. Liu, L. Cheng, J. H. Liang and P. H. Jiang, *J. Mater. Chem. A*, 2018, **6**, 12125–12131.
29 B. Xu, T. Feng, Z. Li, S. T. Pantelides and Y. Wu, *Nano Lett.*, 2018, **18**, 4034–4039.
30 Y. Zheng, Q. Zhang, X. Su, H. Xie, S. Shu, T. Chen, G. Tan, Y. Yan, X. Tang, C. Uher and G. J. Snyder, *Adv. Energy Mater.*, 2015, **5**, 1401391.
31 W. Lee, K. D. Kihm, H. G. Kim, S. Shin, C. Lee, J. S. Park, S. Cheon, O. M. Kwon, G. Lim and W. Lee, *Nano Lett.*, 2017, **17**, 2361–2366.
32 Q. Zhang, Z. Zhou, M. Dylla, M. T. Agne, Y. Pei, L. Wang, Y. Tang, J. Liao, J. Li, S. Bai, W. Jiang, L. Chen and G. Jeffrey Snyder, *Nano Energy*, 2017, **41**, 501–510.
33 M. T. Dylla, J. J. Kuo, I. Witting and G. J. Snyder, *Adv. Mater. Interfaces*, 2019, **6**, 1900222.
34 T. G. Novak, H. Shin, J. Kim, K. Kim, A. Azam, C. V. Nguyen, S. H. Park, J. Y. Song and S. Jeon, *ACS Appl. Mater. Interfaces*, 2018, **10**, 17957–17962.
35 D. Madan, Z. Wang, A. Chen, R.-C. Juang, J. Keist, P. K. Wright and J. W. Evans, *ACS Appl. Mater. Interfaces*, 2012, **4**, 6117–6124.
36 J. Peng, I. Witting, N. Geisendorfer, M. Wang, M. Chang, A. Jakus, C. Kenel, X. Yan, R. Shah, G. J. Snyder and M. Grayson, *Nat. Commun.*, 2019, **10**, 5590.
37 J. Kim, N. M. Han, J. Kim, J. Lee, J.-K. Kim and S. Jeon, *ACS Appl. Mater. Interfaces*, 2018, **10**, 37507–37516.
38 M. Choi, J. Baek, J. Ryu, H. Lee, J. Byen, S.-G. Hong, B. J. Kim, S. Cho, J. Y. Song, G.-H. Lee, H. Shin, J.-Y. Choi and S. Jeon, *Nano Lett.*, 2022, **22**, 5198–5206.
39 D. Han, L. Yan, W. Chen and W. Li, *Carbohydr. Polym.*, 2011, **83**, 653–658.
40 S. Vadukumpully, J. Paul, N. Mahanta and S. Valiyaveettil, *Carbon*, 2011, **49**, 198–205.
41 Y.-X. Yu, *Phys. Chem. Chem. Phys.*, 2013, **15**, 16819–16827.
42 Y.-X. Yu, *J. Mater. Chem. A*, 2014, **2**, 8910–8917.
43 Y. Guo, J. Mu, C. Hou, H. Wang, Q. Zhang and Y. Li, *Carbon*, 2016, **107**, 146–153.
44 H. Sevinçli and G. Cuniberti, *Sci. Rep.*, 2010, **81**, 113401.
45 Q.-Y. Li, T. Feng, W. Okita, Y. Komori, H. Suzuki, T. Kato, T. Kaneko, T. Ikuta, X. Ruan and K. Takahashi, *ACS Nano*, 2019, **13**, 9182–9189.
46 X. Fan, Z. Shen, A. Q. Liu and J.-L. Kuo, *Nanoscale*, 2012, **4**, 2157–2165.
47 K. Yang, Y. Chen, R. D'Agosta, Y. Xie, J. Zhong and A. Rubio, *Phys. Rev. B: Condens. Matter Mater. Phys.*, 2012, **86**, 045425.
48 G. Lim, K. D. Kihm, H. G. Kim, W. Lee, W. Lee, K. R. Pyun, S. Cheon, P. Lee, J. Y. Min and S. H. Ko, *Nanomaterials*, 2018, **8**, 557.
49 G. Rajasekaran, P. Narayanan and A. Parashar, *Crit. Rev. Solid State Mater. Sci.*, 2016, **41**, 47–71.
50 E. Pop, V. Varshney and A. K. Roy, *MRS Bull.*, 2012, **37**, 1273–1281.
51 D. Chen, Y. Zhao, Y. Chen, B. Wang, H. Chen, J. Zhou and Z. Liang, *ACS Appl. Mater. Interfaces*, 2015, **7**, 3224–3230.
52 X. Feng, Y. Fan, N. Nomura, K. Kikuchi, L. Wang, W. Jiang and A. Kawasaki, *Carbon*, 2017, **112**, 169–176.
53 S. Li, T. Fan, X. Liu, F. Liu, H. Meng, Y. Liu and F. Pan, *ACS Appl. Mater. Interfaces*, 2017, **9**, 3677–3685.

54 Y. Liang, C. Lu, D. Ding, M. Zhao, D. Wang, C. Hu, J. Qiu, G. Xie and Z. Tang, *Chem. Sci.*, 2015, **6**, 4103–4108.

55 X. Liu, S. Li, J. Yu, Y. Zhu, K. Lin, B. Wang, R. Cai, D. Ekren, D. Lewis, I. A. Kinloch, M. J. Reece and R. Freer, *Carbon*, 2024, **216**, 118509.

56 T. G. Novak, K. Kim and S. Jeon, *Nanoscale*, 2019, **11**, 19684–19699.

57 T. A. Amollo, G. T. Mola, M. S. K. Kirui and V. O. Nyamori, *Crit. Rev. Solid State Mater. Sci.*, 2018, **43**, 133–157.

58 B. H. Kim, D. C. Kim, M. H. Jang, J. Baek, D. Park, I. S. Kang, Y. C. Park, S. Ahn, Y. H. Cho, J. Kim and S. Jeon, *Adv. Mater.*, 2016, **28**, 1657–1662.

59 S. Kim, S. B. Jo, J. Kim, D. Rhee, Y. Y. Choi, D. H. Kim, J. Kang and J. H. Cho, *Adv. Funct. Mater.*, 2022, **32**, 2111956.

60 X. Li, L. Fan, Z. Li, K. Wang, M. Zhong, J. Wei, D. Wu and H. Zhu, *Adv. Energy Mater.*, 2012, **2**, 425–429.

61 J.-H. Choi, J.-W. Jung, S.-H. Jung, C. Y. Choi, W.-H. Ryu, S.-M. Jo, D.-S. Lim, S. Jeon, H.-M. Lee and I.-D. Kim, *RSC Adv.*, 2016, **6**, 60537–60545.

62 Y. Zhu, S. Murali, W. Cai, X. Li, J. W. Suk, J. R. Potts and R. S. Ruoff, *Adv. Mater.*, 2010, **22**, 3906–3924.

63 P. Avouris and C. Dimitrakopoulos, *Mater. Today*, 2012, **15**, 86–97.

64 K. Novoselov, S. Morozov, T. Mohinddin, L. Ponomarenko, D. C. Elias, R. Yang, I. Barbolina, P. Blake, T. Booth and D. Jiang, *Phys. Status Solidi B*, 2007, **244**, 4106–4111.

65 Y. Anno, Y. Imakita, K. Takei, S. Akita and T. Arie, *2D Mater.*, 2017, **4**, 025019.

66 J. D. Renteria, D. L. Nika and A. A. Balandin, *Appl. Sci.*, 2014, **4**, 525–547.

67 Q. Meng, Y. Yang, S. Han, F. Meng and T. Liu, *Polym. Compos.*, 2024, **45**, 8176–8186.

68 F. N. Ajeel, A. B. Ahmed and A. M. Khudhair, *Nano-Struct. Nano-Objects*, 2024, **38**, 101164.

69 L. Yang, X. Chen, A. Dutta, H. Zhang, Z. Wang, M. Xin, S. Du, G. Xu and H. Cheng, *Nat. Commun.*, 2025, **16**, 792.

70 S.-G. Nam, D.-K. Ki and H.-J. Lee, *Phys. Rev. B: Condens. Matter Mater. Phys.*, 2010, **82**, 245416.

71 J. Duan, X. Wang, X. Lai, G. Li, K. Watanabe, T. Taniguchi, M. Zebarjadi and E. Y. Andrei, *Proc. Natl Acad. Sci. U. S. A.*, 2016, **113**, 14272–14276.

72 M. S. Hossain, D. H. Huynh, P. D. Nguyen, L. Jiang, T. C. Nguyen, F. Al-Dirini, F. M. Hossain and E. Skafidas, *J. Appl. Phys.*, 2016, **119**(12, 125106.

73 J. Lee, J. Baek, G. H. Ryu, M. J. Lee, S. Oh, S. K. Hong, B.-H. Kim, S.-H. Lee, B. J. Cho, Z. Lee and S. Jeon, *Nano Lett.*, 2014, **14**, 4352–4359.

74 J. Baek, M. Lee, J. Kim, J. Lee and S. Jeon, *Carbon*, 2018, **127**, 41–46.

75 E. Lee, J. Baek, J. S. Park, J. Kim, J. M. Yuk and S. Jeon, *2D Mater.*, 2018, **6**, 011001.

76 K. H. Park, B. H. Kim, S. H. Song, J. Kwon, B. S. Kong, K. Kang and S. Jeon, *Nano Lett.*, 2012, **12**, 2871–2876.

77 N. I. Zaaba, K. L. Foo, U. Hashim, S. J. Tan, W.-W. Liu and C. H. Voon, *Procedia Eng.*, 2017, **184**, 469–477.

78 C. Gómez-Navarro, J. C. Meyer, R. S. Sundaram, A. Chuvilin, S. Kurasch, M. Burghard, K. Kern and U. Kaiser, *Nano Lett.*, 2010, **10**, 1144–1148.

79 T. Li, A. D. Pickel, Y. Yao, Y. Chen, Y. Zeng, S. D. Lacey, Y. Li, Y. Wang, J. Dai and Y. Wang, *Nat. Energy*, 2018, **3**, 148–156.

80 N. D. K. Tu, J. Choi, C. R. Park and H. Kim, *Chem. Mater.*, 2015, **27**, 7362–7369.

81 J. Kim, G. Yoon, J. Kim, H. Yoon, J. Baek, J. H. Lee, K. Kang and S. Jeon, *Carbon*, 2018, **139**, 309–316.

82 R. Mulla, A. O. White, C. W. Dunnill and A. R. Barron, *Energy Adv.*, 2023, **2**, 606–614.

83 D. Li, Y. Gong, Y. Chen, J. Lin, Q. Khan, Y. Zhang, Y. Li, H. Zhang and H. Xie, *Nano-Micro Lett.*, 2020, **12**, 1–40.

84 H. Tang, F.-H. Sun, J.-F. Dong, H.-L. Zhuang, Y. Pan and J.-F. Li, *Nano Energy*, 2018, **49**, 267–273.

85 B. Liang, Z. Song, M. Wang, L. Wang and W. Jiang, *J. Nanomater.*, 2013, **2013**, 210767.

86 J.-H. Bahk, Z. Bian and A. Shakouri, *Energy Harvestin.g Syst*, 2013, **87**, 075204.

87 J. W. Lee, E. K. Lee, B. S. Kim, J. H. Lee, H. G. Kim, H. S. Jang, S. W. Hwang, B. L. Choi and D. Whang, *ChemSusChem*, 2015, **8**, 2372–2377.

88 J. Choi, J. Y. Lee, S. S. Lee, C. R. Park and H. Kim, *Adv. Energy Mater.*, 2016, **6**, 1502181.

89 J. U. Rahman, S. Guo, N. Pérez, K. Jang, C. Jung, P. Ying, C. Scheu, D. Zavanelli, S. Zhang and A. Sotnikov, *Adv. Energy Mater.*, 2024, 2404243.

90 T. Q. Kimberly, K. M. Ciesielski, X. Qi, E. S. Toberer and S. M. Kauzlarich, *ACS Appl. Electron. Mater.*, 2024, **6**, 2816–2825.

91 J. Oh, Y. Kim, S. Chung, H. Kim and J. G. Son, *Adv. Mater. Interfaces*, 2019, **6**, 1901333.

92 J. Kim, M. Jung, D. U. Lim, D. Rhee, S. H. Jung, H. K. Cho, H.-K. Kim, J. H. Cho and J. Kang, *Nano Lett.*, 2021, **22**, 570–577.

93 A. K. Gautam, M. Faraz and N. Khare, *J. Alloys Compd.*, 2020, **838**, 155673.

94 S. H. Song, B. H. Kim, D.-H. Choe, J. Kim, D. C. Kim, D. J. Lee, J. M. Kim, K. J. Chang and S. Jeon, *Adv. Mater.*, 2015, **27**, 3152–3158.

95 Y. Kinemuchi, M. Mikami, K. Kobayashi, K. Watari and Y. Hotta, *J. Electron. Mater.*, 2010, **39**, 2059–2063.

96 M. Ruoho, T. Juntunen and I. Tittonen, *Nanotechnology*, 2016, **27**, 355403.

97 S. Jeon, J.-U. Park, R. Cirelli, S. Yang, C. E. Heitzman, P. V. Braun, P. J. A. Kenis and J. A. Rogers, *Proc. Natl. Acad. Sci. U. S. A.*, 2004, **101**, 12428–12433.

98 S.-H. Nam, G. Hyun, D. Cho, S. Han, G. Bae, H. Chen, K. Kim, Y. Ham, J. Park and S. Jeon, *Nano Res.*, 2021, **14**, 2965–2980.

99 G. Bae, D. Jang and S. Jeon, *ACS Nano*, 2021, **15**, 3960–3970.

100 S. H. Nam, J. Park and S. Jeon, *Adv. Funct. Mater.*, 2019, **29**, 1904971.

101 G. Bae, D. G. Kang, C. Ahn, D. Kim, H. G. Nam, G. Hyun, D. Jang, S. M. Han and S. Jeon, *Nano Lett.*, 2024, **24**, 13414–13421.

102 J. Shin, G. Lee, M. Choi, H. Jang, Y. Lim, G.-S. Kim, S.-H. Nam, S.-H. Baek, H.-C. Song, J. Kim, C.-Y. Kang, J.-O. Lee, S. Jeon, D. Cho and J.-S. Jang, *J. Mater. Chem. A*, 2023, **11**(18195), au18206.

103 H. Chen, G. Chang, T. H. Lee, S. Min, S. Nam, D. Cho, K. Ko, G. Bae, Y. Lee, J. Feng, H. Zhang, J. K. Kim, J. Shin, J. W. Hong and S. Jeon, *Nat. Commun.*, 2024, **15**, 8074.

104 J. Lee, H. Lee, T.-H. Bae, D. Cho, M. Choi, G. Bae, Y.-S. Shim and S. Jeon, *Small Struct.*, 2024, **5**, 2300503.

105 H. Chang, S. Kwon, G. Bae and S. Jeon, *Nanophotonics*, 2024, **13**, 971–982.

106 H. Yoon, Y. H. Chang, S. H. Song, E.-S. Lee, S. H. Jin, C. Park, J. Lee, B. H. Kim, H. J. Kang, Y.-H. Kim and S. Jeon, *Adv. Mater.*, 2016, **28**, 5255–5261.

107 S. Lee, J. Lee and S. Jeon, *Sci. Adv.*, 2023, **9**, eade2585.

108 S. H. Song, M. H. Jang, J. Chung, S. H. Jin, B. H. Kim, S. H. Hur, S. Yoo, Y. H. Cho and S. Jeon, *Adv. Opt. Mater.*, 2014, **2**, 1016–1023.

109 H. Ju, D. Park, M. Kim and J. Kim, *J. Mater. Sci. Technol.*, 2022, **129**, 190–195.

110 C. Gayner, R. Sharma, I. Malik, M. Kumar, S. Singh, K. Kumar, J. Tahalyani, T. Srivastava, K. K. Kar and H. Yokoi, *Nano Energy*, 2022, **94**, 106943.

111 F.-P. Du, N.-N. Cao, Y.-F. Zhang, P. Fu, Y.-G. Wu, Z.-D. Lin, R. Shi, A. Amini and C. Cheng, *Sci. Rep.*, 2018, **8**, 6441.

112 L. Wang, Q. Yao, H. Bi, F. Huang, Q. Wang and L. Chen, *J. Mater. Chem. A*, 2015, **3**, 7086–7092.

113 Y. Lin, C. Norman, D. Srivastava, F. Azough, L. Wang, M. Robbins, K. Simpson, R. Freer and I. A. Kinloch, *ACS Appl. Mater. Interfaces*, 2015, **7**, 15898–15908.

114 M. S. El-Asfoury, M. N. A. Nasr, K. Nakamura and A. Abdel-Moneim, *J. Alloys Compd.*, 2018, **745**, 331–340.

115 O. Okhay, S. Zlotnik, W. Xie, K. Orlinski, M. J. H. Hortiguela Gallo, G. Otero-Irurueta, A. J. S. Fernandes, D. A. Pawlak, A. Weidenkaff and A. Tkach, *Carbon*, 2019, **143**, 215–222.

116 W. H. Nam, Y. S. Lim, W. Kim, H. K. Seo, K. S. Dae, S. Lee, W.-S. Seo and J. Y. Lee, *Nanoscale*, 2017, **9**, 7830–7838.

117 S. Yadav, S. Chaudhary and D. K. Pandya, *Ceram. Int.*, 2018, **44**, 10628–10634.

118 C. Wu, J. Li, Y. Fan, J. Xing, H. Gu, Z. Zhou, X. Lu, Q. Zhang, L. Wang and W. Jiang, *J. Alloys Compd.*, 2019, **786**, 884–893.

119 X. Liang, Y. Yang, F. Dai and C. Wang, *J. Mater. Chem. C*, 2019, **7**, 1208–1221.

120 J. Kim, J. Kim, S. Song, S. Zhang, J. Cha, K. Kim, H. Yoon, Y. Jung, K.-W. Paik and S. Jeon, *Carbon*, 2017, **113**, 379–386.